Journal of Engineering Mathematics (2026) 158:3
https://doi.org/10.1007/s10665-026-10521-7

Modal analysis of a mooring line with rigorous seabed condition

Pietro Prestininzi[1] · **Giampiero Sciortino**[1]

Received: 15 January 2026 / Accepted: 7 April 2026

Abstract

The location of the Touch Down Point (TDP) of a slack mooring line, closely linked to its residual resistance, requires accurate modeling. We introduce an analytical formulation of seabed contact dynamics as a rigorous boundary condition for the system. Building on this, a modal analysis is developed to fully characterize the natural oscillation modes of a slack mooring line without assumptions on tension perturbations. The framework captures the dynamics of the moving boundary at the seabed and establishes a direct link between the maximum oscillation amplitudes and the onset of shock formation at the contact point. A complementary formulation describes, in static or quasi-static regimes, the relationship between fairlead displacement and seabed contact point motion, providing a solid basis for the study of seabed interaction mechanics. Finally, a numerical investigation contrasts the proposed exact seabed boundary condition with a widely used empirical approximation. The comparison is carried out against two exact benchmarks: (i) natural frequencies from modal analysis and (ii) analytically derived seabed contact point displacement under steady fairlead tension. Results confirm that the new boundary condition improves predictive accuracy without added computational cost. These findings advance the understanding of slack-line dynamics and support future analytical and numerical studies.

Keywords CALM · Modal analysis · Mooring line · Seabed contact point · Touch Down Point

Pietro Prestininzi and Giampiero Sciortino contributed equally to this work.

✉ Pietro Prestininzi
pietro.prestininzi@uniroma3.it

Giampiero Sciortino
giampiero.sciortino@uniroma3.it

[1] Department of Civil Engineering, Computer Science and Aeronautical Technologies, Roma Tre University, Via Vito Volterra 62, 00146 Rome, Italy

Published online: 13 May 2026

1 Introduction

The dynamic behavior of mooring lines is a subject of longstanding importance in offshore engineering due to its impact on station-keeping performance and system integrity. Mooring lines are often subjected to large displacements, nonlinear hydrodynamic forces, and complex seabed interactions, whose first modeling attempts can be traced back to [1, 2]. The topic has remained active through decades, motivated by the need for increasingly accurate models able to tackle demanding multidirectional sea state forcings, complex bathymetries, and multiple mooring line arrangements [3–9]. An even stronger scientific interest in the subject has been recently catalyzed by the need to provide reliable mooring modules to support the design of offshore wind turbines. Several modern numerical frameworks include coupling between mooring and floating body dynamics, acknowledging the bidirectional feedback inherent to such systems [10, 11]. Historical failures in permanent mooring systems further underscore the need for accurate modeling techniques [12, 13]. Such detailed reviews of integrity issues provide valuable insights into how improper representation of dynamic effects, particularly in the touchdown region, has contributed to system malfunction.

Time domain approaches, despite their heavier computational burden, have been preferred over the more agile frequency domain approaches [11, 14] due to their ability to handle strong nonlinearities. The mathematical treatment of these problems has also been supported by foundational works on cable dynamics [15] and mooring system theory [16]. Numerous numerical investigations into time integration schemes have clarified the accuracy and stability of solvers applied to mooring dynamics [17], and comprehensive PhD studies have deepened our understanding of geometric nonlinearity and compliant mooring systems [18]. Laboratory investigations into the top-end (fairlead) motion and its influence on cable response have validated numerical models under controlled conditions [19].

Though both experimental and numerical studies continue to refine our understanding of mooring dynamics, the modal analysis of a mooring line has been overlooked. Indeed, the knowledge of the natural frequencies of oscillation of the mooring line is of pivotal importance for modeling the oscillating behavior of an offshore floater. In broader contexts, the natural oscillations of catenary lines have been considered for slack-sag layouts [20, 21], and in other fields [22].

Such studies, however, do not take into account the peculiar boundary condition of the Touch Down Point (TDP) of mooring lines, where line–seabed interaction occurs, despite several works highlighting that dynamic effects in the touchdown zone significantly affect the global behavior of mooring systems [5, 23]. Recent works compare modeling techniques and highlight the sensitivity of results to seabed contact formulations, showing that empirical contact models may underpredict critical loads and modes [8, 23]. Nonlinear time-domain analyses incorporating seabed contact have been developed for various line configurations and environmental conditions [3, 24]. Advanced numerical strategies such as hp-adaptive discontinuous Galerkin methods [25] and high-order finite-volume approaches [26] have proven effective in resolving dynamic snap loads and capturing sharp gradients in tension and curvature.

In this context, the main novelty of the present work lies in the development of a modal analysis that explicitly accounts for the TDP condition by incorporating the

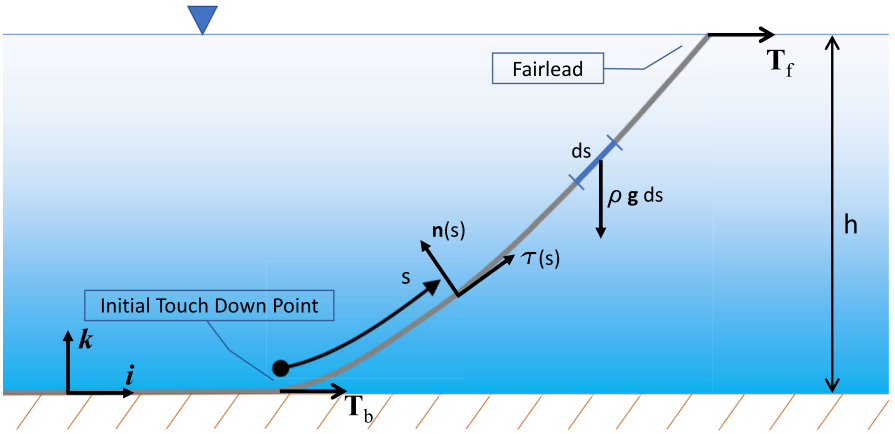

Fig. 1 Sketch of the conceptual model of the mooring line adopted in this study

local geometric configuration of the line. This approach enables the formulation of a differential equation governing the motion of the TDP, effectively treating it as a moving boundary whose evolution depends on the solution itself. We compare our approach with widely adopted empirical contact models for the seabed interaction and analyze the resulting modal properties. We derive reference data from the numerical integration of both the dynamic and static systems. The focus is placed on investigating how seabed modeling assumptions may influence the natural frequencies, mode shapes, and stability margins of the mooring system, an aspect that has received limited attention in the literature.

2 Mathematical modeling

In this section, we provide a comprehensive description of the mathematical framework employed in this study. We start by writing the dynamic equations of a line moving in the vertical plane; then we derive their static counterpart.

2.1 Dynamic equations of 2D mooring line

We consider an inextensible line with negligible bending moment moving within the $x-z$ plane, being $\mathbf{i}-\mathbf{k}$ the associated unit vectors. A curvilinear abscissa s is defined along the line at the initial time. The configuration of the line at time t can be conveniently described by the parametric vector function $\mathbf{X}(s,t) = x(s,t)\mathbf{i}+z(s,t)\mathbf{k}$. In the following, subscripts s and t will be used as spatial and time derivatives, respectively. If the quantity s also defines the position of a material point, the inextensibility assumption is tantamount to requiring $\forall t : \mathbf{X}_s \cdot \mathbf{X}_s = 1$.

With reference to Fig. 1, the integral balance equation of linear momentum for the line segment between s_b and s can be written as follows:

$$T(s,t)\boldsymbol{\tau}(s,t) - T(s_\mathrm{b},t)\boldsymbol{\tau}(s_\mathrm{b},t) + - \int_{s_\mathrm{b}}^{s} \left(\rho\mathbf{f} - \rho_\mathrm{f} A_\mathrm{f} g\mathbf{k} - \frac{1}{2}\rho_\mathrm{f} C_D d_\mathrm{eq} |\mathbf{X}_\mathrm{t}| \mathbf{X}_t\right) \mathrm{d}\lambda$$
$$= \partial/\partial t \int_{s_\mathrm{b}}^{s} (\rho + m_\mathrm{a})\, \mathbf{X}_t(\lambda,t)\mathrm{d}\lambda, \tag{1}$$

where s_b is the curvilinear abscissa of the material point of contact with the seabed (briefly the TDP), $\mathbf{f}$ is the external force per unit mass, ρ is the linear mass density, $T(s,t)$ is the scalar tension field, $\boldsymbol{\tau} = x_\mathrm{s}\mathbf{i} + z_\mathrm{s}\mathbf{k}$ is the tangent unit vector, ρ_f is the fluid density, A_f is the line volume per unit length, C_D is the drag coefficient, d_eq is the diameter of the equivalent "dragging" cylindrical cable, and m_a is the added mass per unit length, assuming an isotropic-added mass tensor. Under the assumptions that buoyancy is negligible with respect to the body-force term, added mass effects are negligible with respect to the structural inertia, and dissipative drag effects are neglected, namely $\rho \gg \rho_\mathrm{f} A_\mathrm{f}$, $\rho \gg m_\mathrm{a}$, Eq. 1 reduces, upon differentiation with respect to s, to the local form which, once coupled with the inextensibility constraint, furnishes the following:

$$\begin{aligned} \rho\mathbf{f} + (T\boldsymbol{\tau})_\mathrm{s} &= \rho\mathbf{X}_\mathrm{tt}, \\ \mathbf{X}_\mathrm{s}\cdot\mathbf{X}_\mathrm{s} &= 1. \end{aligned} \tag{2}$$

By performing the same spatial differentiation on the tension field in Eq. 2, we obtain the following: $\rho\mathbf{f} + T_\mathrm{s}\boldsymbol{\tau} + T\mathbf{n}/R = \rho\mathbf{X}_\mathrm{tt}$, where $\mathbf{n} = (-z_\mathrm{s}\mathbf{i} + x_\mathrm{s}\mathbf{k})$ is the normal unit vector, $R = 1/\vartheta_\mathrm{s}$ is the radius of curvature, being $\vartheta = \arcsin(z_\mathrm{s})$ which leads to $R = \sqrt{1 - z_\mathrm{s}^2}/z_\mathrm{ss}$.

Projecting the first of Eq. 2 along x and z, we obtain the following:

$$\begin{aligned} \rho f^{(x)} + T_\mathrm{s} x_\mathrm{s} - T z_\mathrm{s}/R &= \rho x_\mathrm{tt}, \\ \rho f^{(z)} + T_\mathrm{s} z_\mathrm{s} + T x_\mathrm{s}/R &= \rho z_\mathrm{tt}, \\ x_\mathrm{s}^2 + z_\mathrm{s}^2 &= 1, \end{aligned} \tag{3}$$

where $f^{(x)}$ and $f^{(z)}$ are the x and z components of the external force. Enforcing the inextensibility condition, the radius of curvature can be expressed as $R \equiv x_\mathrm{s}/z_\mathrm{ss}$; by multiplying the first two of Eq. 3 by x_s and z_s, respectively, summing them and exploiting the inextensibility condition, we obtain the non-evolutionary equation for the tension field:

$$T_\mathrm{s} = \rho\left[x_\mathrm{s}(x_\mathrm{tt} - f^{(x)}) + z_\mathrm{s}(z_\mathrm{tt} - f^{(z)})\right]. \tag{4}$$

2.2 Boundary conditions: seabed contact and fairlead points

2.2.1 Condition at the seabed

Burridge and Keller [2] demonstrated that the line at the seabed ($s = s_\mathrm{b}(t)$) exhibits a horizontal tangent, i.e., $\boldsymbol{\tau}(s_\mathrm{b}, t) = \boldsymbol{i}$, provided the TDP moves more slowly than the wave celerity along the line, namely $|s_\mathrm{b}'(t)| < \sqrt{T_\mathrm{b}/\rho}$, where $T_\mathrm{b} = T(s_\mathrm{b}, t)$ denotes the tension at the seabed and the prime indicates ordinary differentiation. All the numerical simulations described in Sect. 7.2 are performed under conditions fully compliant with the above requirement. By imposing the vertical component of the tangent unit vector vanishes, namely,

$$z_\mathrm{s}(s_\mathrm{b}(t), t) = 0, \tag{5}$$

differentiating the latter with respect to time: $\mathrm{d}/\mathrm{d}t\, z_\mathrm{s}(s_\mathrm{b}(t), t) = z_{\mathrm{s,s}}(s_\mathrm{b}(t), t)s_\mathrm{b}'(t) + z_{\mathrm{s,t}}(s_\mathrm{b}(t), t) = 0$, we can derive a differential law for the position of the TDP point:

$$s_\mathrm{b}'(t) = -z_{\mathrm{s,t}}(s_\mathrm{b}(t), t)/z_{\mathrm{s,s}}(s_\mathrm{b}(t), t), \tag{6}$$

which needs to be coupled with an additional condition stating the equivalence between the TDP position and the curvilinear abscissa:

$$x(s_\mathrm{b}(t), t) = s_\mathrm{b}(t). \tag{7}$$

2.2.2 Condition at the fairlead

Assuming no vertical motion of the fairlead ($s = s_\mathrm{f}$), i.e., we can impose either a time history of the horizontal tension $T_\mathrm{f}(t)$ together with a fixed value for z or a prescribed horizontal motion. The former is employed here, namely,

$$\begin{aligned} z(s_\mathrm{f}, t) &= h, \\ T(s_\mathrm{f}, t)x_\mathrm{s}(s_\mathrm{f}, t) &= T_\mathrm{f}(t). \end{aligned} \tag{8}$$

It is worth mentioning that the local motion laws (Eq. 2) and the condition at the fairlead (second of Eq. 8) can be derived from the principle of least action. Conversely, the TDP condition does not emerge naturally from such approach, and needs to be prescribed externally of the variational principle. Details on such alternative approach are reported in Appendix A.

2.3 Static equations: the catenary shape

The static counterpart of the problem at hand can be obtained by multiplying the first two of Eq. 3, respectively, for x_s and z_s, dropping the time derivatives and considering

only gravity as the external force:

$$\begin{aligned} T'x'^2 - Tz'z'' &= 0, \\ T'z'^2 + Tz'z'' &= \rho g z', \\ (x')^2 + (z')^2 &= 1, \end{aligned} \tag{9}$$

where g is the acceleration due to gravity. By adding the first two of Eq. 9, substituting the third and integrating, we can obtain the tension distribution as a function of $z(s)$: $T' = \rho g z' \longrightarrow T = \rho g z + T_\mathrm{b}$. Note that, at this stage, no assumption has been made about the shape of the line at the point of contact with the seabed. By substituting into the first of Eq. 9, we have

$$\rho g z' x'^2 - T z' z'' = 0,$$

from which we can solve for $x' = \sqrt{\frac{T}{\rho g} z''}$ and plug it into the second of Eq. 9: $z'^2 + \left(z + \frac{T_\mathrm{b}}{\rho g}\right) z'' = 1$, which is an ordinary differential equation in the unknown $z(s)$. By imposing two conditions for z at the TDP, namely $z(0) = 0$ and $z'(0) = 0$, and $x(0) = 0$ for x, together with the third of Eq. 9, the following analytical parametric solutions are obtained:

$$\begin{aligned} z(s) &= \sqrt{s^2 + \chi^2} - \chi \equiv Z_0(s) \\ x(s) &= \chi \sinh^{-1}(s/\chi) \equiv X_0(s), \end{aligned} \tag{10}$$

where $\chi = T_\mathrm{b}/(\rho g)$. The classical Cartesian form of the catenary is obtained by eliminating s in Eq. 10.

3 Modal analysis

With the aim of focusing on the effect of the modeling of the TDP boundary condition, we limit the external forces acting on the line to gravity; thus, Eq. 2 can be written as follows:

$$\begin{aligned} T_\mathrm{s} x_\mathrm{s}^2 - T z_\mathrm{s} z_\mathrm{ss} - \rho x_\mathrm{s} x_\mathrm{tt} &= 0, \\ -\rho z_\mathrm{s} g + T_\mathrm{s} z_\mathrm{s}^2 + T z_\mathrm{s} z_\mathrm{ss} - \rho z_\mathrm{s} z_\mathrm{tt} &= 0, \\ x_\mathrm{s}^2 + z_\mathrm{s}^2 - 1 &= 0. \end{aligned} \tag{11}$$

The static solution $(X_0(s), Z_0(s), T_0(s))$ can be perturbed as follows:

$$\begin{aligned} x(s,t) &= X_0(s) + \varepsilon X(s) \mathrm{e}^{I\omega t} \\ z(s,t) &= Z_0(s) + \varepsilon Z(s) \mathrm{e}^{I\omega t} \\ T(s,t) &= T_0(s) + \varepsilon T(s) \mathrm{e}^{I\omega t}, \end{aligned} \tag{12}$$

where ε is a small nondimensional quantity, I is the imaginary unit. By substituting Eq. 12 into Eq. 11, recalling that static solution satisfies Eq. 9, dropping

higher-order terms in ε, we come to a homogeneous ODE system in the unknowns $(X(x), Z(s), T(s))$:

$$\begin{aligned} X_0'\left(\rho\omega^2 X + 2T_0'X' + T'X_0'\right) - T_0Z_0'Z'' - \left(T_0Z' + TZ_0'\right)Z_0'' &= 0,\\ Z_0'\left(\rho\omega^2 Z + T'Z_0' + T_0Z'' + TZ_0''\right) + Z'\left(-\rho g + 2T_0'Z_0' + T_0Z_0''\right) &= 0,\\ X''X_0' + X'X_0'' + Z''Z_0' + Z'Z_0'' &= 0, \end{aligned} \tag{13}$$

where the last equation is obtained by perturbing the derivative of the third of Eq. 11. By algebraic manipulations, we can cast system (13) into the following form:

$$\begin{aligned} -X_0'(2T_0'X' + T_0X'') - T_0X_0''X' - \left(T'X_0'^2 - TZ_0'Z_0''\right) &= \lambda(\rho X_0')X\\ -Z_0'T_0Z'' - Z'(-\rho g + 2T_0'Z_0' + T_0Z_0'') - \left(T'Z_0'^2 + TZ_0'Z_0''\right) &= \lambda(\rho Z_0')Z\\ -(T' - \rho gZ') &= \lambda\rho(X_0'X + Z_0'Z), \end{aligned} \tag{14}$$

where $\lambda = \omega^2$. The eigenvalue problem (14), in the unknowns $(\lambda, X(s), Z(s), T(s))$, is non-standard, since the term $\lambda T(s)$ is missing on the right-hand side of the third equation: this feature will need to be handled properly when tackling the problem numerically.

3.1 Boundary conditions for the perturbed solutions

3.1.1 Condition at the seabed

In the following, we will substitute the perturbed solution (12) into both boundary conditions (6) and (5). Expanding around $s = 0$, we get

$$s_b'(t) = \frac{-\varepsilon I\omega Z'(s_b(t))e^{I\omega t}}{Z_0''(s_b(t)) + \varepsilon Z''(s_b(t))e^{I\omega t}} = \frac{-\varepsilon I\omega Z'(0)e^{I\omega t}}{Z_0''(0)} + O(\varepsilon^2), \tag{15}$$

Integrating once, discarding higher-order terms, and recalling that the static solution satisfies the relation $Z_0''(0) = \chi^{-1}$, we can write the following:

$$s_b(t) = -\chi\varepsilon Z'(0)e^{I\omega t}, \tag{16}$$

which states that the TDP point of the perturbed solution inherits its harmonic form from the perturbation. If we require the perturbed solution $Z_0(s) + \varepsilon Z(s)e^{I\omega t}$ to fulfill the first of the seabed conditions $z(s_b(t), t) = 0$, we obtain

$$Z_0(s_b(t)) + \varepsilon Z(s_b(t))e^{I\omega t} = 0$$

which can be expanded as

$$Z_0(0) + Z_0^{'}(0)s_\mathrm{b}(t) + \varepsilon Z(0)\mathrm{e}^{I\omega t} + O(\varepsilon^2) = 0,$$

and, recalling that $Z_0(0) = 0$, $Z_0^{'}(0) = 0$, we conclude that, at first order in ϵ

$$Z(0) = 0. \tag{17}$$

Now we substitute the perturbed solution into the boundary condition (5) which yields $Z_0'(s_\mathrm{b}(t)) + \varepsilon Z'(s_\mathrm{b}(t))\mathrm{e}^{I\omega t} = 0$, expanding around $s = 0$ and retaining only lower-order terms, we obtain $Z_0'(0) + Z_0''(0)s_\mathrm{b}(t) + \varepsilon Z'(0)\mathrm{e}^{I\omega t} + O(\varepsilon^2) = 0$. Recalling that $Z_0'(0) = 0$ and using Eq. 16 we have $0 = (-Z_0''(0)\chi + 1)\varepsilon Z'(0)\mathrm{e}^{I\omega t} = (-\chi^{-1}\chi + 1)\varepsilon Z'(0)\mathrm{e}^{I\omega t} = 0$. The resulting identity suggests that, as per the perturbation function, no zero derivative needs to be enforced at the seabed contact point. Instead, since the whole perturbed solution still features a horizontal tangent at the seabed contact point, the condition in Eq. 7 must be enforced on the perturbed solution as well, leading to $X_0(s_\mathrm{b}(t)) + \varepsilon X(s_\mathrm{b}(t))\mathrm{e}^{I\omega t} = s_\mathrm{b}(t)$ again, expanding around $s = 0$: $X_0(0) + X_0'(0)s_\mathrm{b}(t) + \varepsilon X(0)\mathrm{e}^{I\omega t} + O(\varepsilon^2) = s_\mathrm{b}(t)$ and recalling that $X_0(0) = 0$, $X_0'(0) = 1$, and truncating higher-order terms:

$$X(0) = 0, \tag{18}$$

which, together with Eq. 17, states that the perturbed solution, at first order, must comply with a seabed boundary condition analogous to that of the taut-line configuration, i.e., a line whose endpoint is fixed to the seabed. For what regards the boundary condition for the tension field, by calculating Eq. 4 at $s = s_\mathrm{b}$, and imposing that $x_s(s_\mathrm{b}(t), t) = 1$ and $z_s(s_\mathrm{b}(t), t) = 0$, we obtain $T_\mathrm{s}(s_\mathrm{b}(t), t) = \rho x_{\mathrm{t,t}}(s_\mathrm{b}(t), t)$. We can then plug the perturbed solutions (Eq. 12) into the latter, resulting in $T_0'(s_\mathrm{b}(t)) + \varepsilon T'(s_\mathrm{b}(t))\mathrm{e}^{I\omega t} = -\rho\omega^2\varepsilon X(s_\mathrm{b}(t))\mathrm{e}^{I\omega t}$. Expanding and retaining lower-order terms, as done previously, we obtain $T_0'(0) + T_0''(0)(-\chi\varepsilon Z'(0)\mathrm{e}^{I\omega t}) + \varepsilon T'(0)\mathrm{e}^{I\omega t} + \rho\omega^2\varepsilon X(0)\mathrm{e}^{I\omega t} = 0$. Recalling that $T_0'(0) = 0$, $T_0''(0) = \rho g\chi^{-1}$ and enforcing the requirement (18) yields

$$-\rho g Z'(0) + T'(0) + \rho\omega^2 X(0) = -\rho g Z'(0) + T'(0) = 0. \tag{19}$$

3.1.2 Condition at the fairlead

We now formulate the conditions for the fairlead boundary. Requiring the perturbed solution to retain a constant height at the fairlead $Z_0(s_\mathrm{f}) + \varepsilon Z(s_\mathrm{f})\mathrm{e}^{I\omega t} = h$. Since $Z_0(s_\mathrm{f}) = h$, we obtain

$$Z(s_\mathrm{f}) = 0. \tag{20}$$

The same approach can be applied to $T(s_\mathrm{f}, t)x_\mathrm{s}(s_\mathrm{f}, t) = T_\mathrm{f}(t)$ yielding $\left(T_0(s_\mathrm{f}) + \varepsilon T(s_\mathrm{f})\mathrm{e}^{I\omega t}\right)\left(X_0'(s_\mathrm{f}) + \varepsilon X'(s_\mathrm{f})\mathrm{e}^{I\omega t}\right) = T_\mathrm{f}$. Recalling that the right-hand side satisfies $T_\mathrm{f} = T_0(s_\mathrm{f})X_0'(s_\mathrm{f})$, at lower order in ε, it can be simplified as follows:

$$T_0(s_\mathrm{f})\varepsilon X'(s_\mathrm{f})\mathrm{e}^{I\omega t} + \varepsilon T(s_\mathrm{f})\mathrm{e}^{I\omega t}X_0'(s_\mathrm{f}) = 0. \tag{21}$$

In summary, all the homogeneous boundary conditions formulated so far are

$$\begin{aligned} Z[0] = 0,\, X[0] = 0,\, -T'(0) + \rho g Z'(0) = 0, \\ T_0(s_\mathrm{f}) X'(s_\mathrm{f}) + T(s_\mathrm{f}) X_0'(s_\mathrm{f}) = 0,\, Z(s_\mathrm{f}) = 0, \end{aligned} \tag{22}$$

which are the sought five conditions required to correctly pose the system of two second-order ODEs in X and Z, coupled with a first-order one in T.

It is worth noting that, for the case of fixed seabed contact point (taut-line), the above conditions still apply. Indeed, the different modal response of the taut-line, with respect to the slack configuration, is determined by the different shapes of the X_0, Z_0, T_0 which, in the taut configuration, do not necessarily require the line to be tangent to the seabed.

4 Nondimensional form of the equations

In this section, we derive the nondimensional form of the previously introduced equations, which will be subjected to analytical and/or numerical solution. We will adopt $\{\rho, g, L_0\}$ as the set of reference quantities, where L_0 is the length of the hanging portion of the static line. Hereinafter, for the sake of readability, all previously defined symbols will also denote the corresponding nondimensional quantities. Summarizing, $s \to s/L_0$, $\mathbf{X} \to \mathbf{X}/L_0$, while time will be made nondimensional through $t \to t/\sqrt{L_0/g}$ and tension through $T \to T/(\rho g L_0)$. It is worth highlighting that the nondimensional curvilinear abscissa s now varies within the range $[0,\ 1]$.

4.1 The dynamic equations

The nondimensional counterpart of Eq. 2, with $\mathbf{f} = -g\mathbf{k}$, reads

$$\begin{aligned} -\boldsymbol{k} + (T\boldsymbol{\tau})_\mathrm{s} &= \mathbf{X}_\mathrm{tt} \\ \mathbf{X}_\mathrm{s} \cdot \mathbf{X}_\mathrm{s} &= 1. \end{aligned} \tag{23}$$

4.2 The static equations

The static solution for the slack configuration depends only on one parameter, namely, $\Gamma = T_\mathrm{b}/(\rho g L_0)$:

$$\begin{aligned} Z_0(s) &= \sqrt{s^2 + \Gamma^2} - \Gamma \\ X_0(s) &= \Gamma \sinh^{-1}(s/\Gamma). \\ T_0(s) &= \Gamma + Z_0(s). \end{aligned} \tag{24}$$

Conversely, the taut configuration can be formulated as a boundary value problem by fixing only the position of the TDP to the seabed ($z(0) = 0$) and the height of the fairlead point ($z(1) = \beta^{-1}$). Solving Eq. 9 with such boundary conditions by means of standard Wolfram Mathematica solvers yields the following solution, expressed as

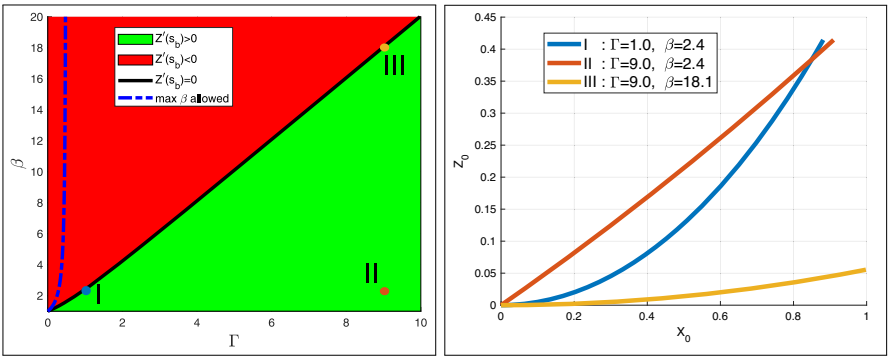

Fig. 2 Left panel: map of all possible static line configurations as function of the two nondimensional state variables; right panel: three line configurations sampled at the three locations in the map

a function of Γ and $\beta = L_0/h \geq 1$:

$$\begin{aligned} Z_{0\text{taut}}(s) &= \sqrt{s^2 + \Gamma^2 + s(\beta^{-2} + 2\beta^{-1}\Gamma - 1)} - \Gamma \\ X_{0\text{taut}}(s) &= \frac{\sqrt{(\beta^2-1)(1+\beta(2\Gamma+1))(1+\beta(2\Gamma-1))}}{2\beta^2} \cdot \\ &\quad \ln\left[\frac{(1+\beta(2\Gamma+1))(\beta-1)}{\beta(\beta(1-2s) - 2\Gamma + 2\beta(Z_{0\text{taut}}(s)+\Gamma)) - 1}\right] \\ T_{0\text{taut}}(s) &= \Gamma + Z_{0\text{taut}}(s). \end{aligned} \tag{25}$$

Solution (25) reduces to solution (24) when the following relation holds:

$$\beta = \sqrt{1+\Gamma^2} + \Gamma. \tag{26}$$

In the $\Gamma - \beta$ plane (see left panel of Fig. 2), all static configurations can be classified into two regions based on the sign of the line slope at the seabed location: positive (green region) and negative (red region, sagline configuration, inadmissible for a horizontal seabed). The boundary between the two regions is described by Eq. 26 and represents all the possible configurations with a horizontal tangent at the seabed. Note that, for the solution given in Eq. 25 to be valid, the parameter β needs to be further constrained by the relation $\beta^{-1} + 2\Gamma > 1$, which defines the region below the blue dashed trace in the left panel of Fig. 2.

Let us define $\tilde{\alpha}$ as the angle between the seabed and the segment passing through the two line extrema for the static slack configuration. Its formulation can be deduced straightforwardly from Eq. 24 and reads

$$\tilde{\alpha} = \operatorname{arccot}\left[\Gamma\left(\Gamma + \sqrt{1+\Gamma^2}\right)\operatorname{arccsch}(\Gamma)\right]. \tag{27}$$

In the following, the above static angle will be compared to its dynamic counterpart.

4.3 The modal equations

The nondimensional version of the system (14) is

$$\begin{aligned}
&- X_0'(2T_0'X' + T_0X'') - T_0X_0''X' - \left[T'X_0'^2 - TZ_0'Z_0''\right] \quad = \lambda(X_0')X \\
&- Z_0'T_0Z^{''} - Z'\left(-1 + 2T_0'Z_0' + T_0Z_0''\right) \\
&- \left[T'Z_0'^2 + TZ_0'Z_0''\right] = \lambda(Z_0')Z \\
&- (T' - Z') = \lambda(X_0'X + Z_0'Z),
\end{aligned} \tag{28}$$

where $\lambda = \omega^2$ has been made nondimensional through g/L_0. The nondimensional forms of the boundary conditions are

$$\begin{aligned}
&X(0) = 0,\ Z(0) = 0,\ T'(0) - Z'(0) = 0 \\
&T_0(1)X'(1) + T(1)X_0'(1) = 0,\ Z(1) = 0.
\end{aligned} \tag{29}$$

It is worth recalling that, when the modal analysis is to be carried out for the taut-line configuration, the static functions given in Eq. 25 must be used in Eqs. 28 and 29.

Neglecting the tension perturbation with respect to the static value (i.e., $T \ll T_0$), and thus dropping all terms in square brackets in Eq. 28, one can decouple the system (28), and solve the resulting second-order ODE for X. Such modeling approach, sometimes referred to as the quasi-steady assumption, is analogous to the one employed by [15, 19], and will be assessed in the following.

5 Numerical solution of the modal equations

A second-order finite difference approach has been employed to numerically solve the eigenproblem (28) coupled with the boundary conditions in Eq. 29. The analytic forms of the static solutions, either Eqs. 24 or 25, have been used to evaluate the coefficients appearing in Eq. 28. Discretizing the vector-valued eigenfunction $(X(s), Z(s), T(s))$ uniformly in the domain $[0, 1] \ni s$ the following generalized eigenproblem arises in finite dimensions:

$$A \cdot W = \lambda B \cdot W, \tag{30}$$

where W is the eigenvector, λ is the eigenvalue, A, B are real-valued square matrices of order $3N$, being N the number of discrete nodes ($N = 200$ has been employed throughout the whole analysis). The non-evolutionary nature of the inextensibility constraint does not allow for a time derivative of the tension to appear as $\lambda T(s)$ at RHS of the third of Eq. 28. Consequently, the matrix B in Eq. 30 results singular. The vector W contains the unknown values at the computational nodes, namely, $W = \left[X^{(i)}, Z^{(i)}, T^{(i)}\right]\ \ i = 1 \ldots N$ Applying a singular value decomposition to B, the system (30) can be rewritten as $U^T.A.W = \lambda D_{\mathrm{I}}.V^T.W$, where U, V are orthonormal matrices, so that $V^T = V^{-1}$ and $U^T = U^{-1}$, and D_{I} is a diagonal matrix. Defining $Y = V^T.W$, and $A_{\mathrm{d}} \equiv U^T.A.V$, the eigenproblem can be cast into the following

form:

$$A_{\mathrm{d}}.Y = \lambda D_{\mathrm{I}}.Y. \tag{31}$$

The resulting eigenproblem (31), while still sharing the same vector of eigenvalues λ with the system (30), is still non-standard, since D_{I} is not the identity matrix. Nonetheless, the form (31) is computationally more advantageous, and has been solved by means of the Arnoldi method [27] .

6 Numerical solution of the dynamic equations

For the numerical solution of the system (23), a second-order in space, finite difference scheme is employed over a uniform grid. The first two of Eq. 23 are solved by means of a time marching, explicit, three-level, second-order in time scheme. The enforcement of the inextensibility condition is achieved by annealing the above time marching scheme in an iterative relaxation procedure which corrects both the local configuration of the line and the tension until the inextensibility is fulfilled within a prescribed precision. The aforementioned numerical scheme, implemented in MATLAB without any specific code optimizations, requires approximately 3 h of computation time to perform 10^6 time steps on a grid comprising 100 nodes when executed on a standard desktop computer. This approach is somehow similar to the one employed in [24].

Regarding the seabed boundary condition, either the rigorous condition (Eq. 6) or the commonly employed empirical description of the contact point is used in the simulations; both have been integrated in the same code. The former is implemented by continuously resizing the numerical domain to account for the movement of the TDP, and thus solving Eq. 23 only on the portion of the line above the seabed elevation. In particular, the displacement of the TDP is predicted by solving the ODE (6) by means of a first-order explicit method. The new position of the TDP is treated as the updated location for the boundary condition, effectively rendering the approach a 1D PDE solver with a solution-dependent moving boundary.

The latter condition, instead, solves for all points of the line, including the ones resting on the seabed. Should the elevation of a point fall below the level of the local seabed, it is set to the seabed height. The position of the TDP is then assumed to correspond to the first point which lies above the seabed height.

7 Results

7.1 Eigenmodes shapes and natural frequencies

In Fig. 3, we show the first three modal shapes resulting from the solution of Eq. 28, as well as the eigenmode for the tension along the line. The magnitude of the perturbation, shared by all three shapes, has been chosen to ensure a clearly visible departure of each eigenmode from the corresponding static configuration.

The numerical solution of the modal Eq. 28 requires, for the slack-line configuration, the specification of either the parameter Γ or β. A wide range of β values, $\beta \in$

[1.1, 8], was finely sampled. For each value, the natural frequencies ω of the first three modes were numerically computed including the simplified model that neglects the perturbations of T with respect to the static ones. It is worth recalling that such approximation is obtained by dropping the terms in square brackets in Eq. 28. As shown in Fig. 4, all frequencies ω increase with β, though at a decreasing rate, $\omega''(\beta) < 0$, since larger β corresponds to larger Γ and, therefore, to higher static tensions. Moreover, the approximate model consistently and significantly underestimates the correct values across the entire β range considered. As $\beta \to 1$ the numerical solution becomes increasingly harder, since high line curvature localized at the TDP requires progressively finer grids. However, it is interesting to inspect the limit behavior of the static system as $\beta \to 0$. In such limit, $X_0 \to 0$, $Z_0 \to s$, $T_0 \to s$ which, once plugged into Eq. 28, reduce the first equation to an identity, and the whole eigenproblem becomes degenerate, which features the following trivial solutions: $\lambda \to$ arbitrary, $X \to$ arbitrary, $Z = 0$, $T = \text{const}$

7.1.1 Shock-free natural oscillations

It is of notable interest to discuss under which conditions the assumption of a horizontal tangent at the TDP holds within the framework of modal analysis. Indeed, as mentioned in Sect. 2.2.1, a departure from such conditions occurs when the TDP velocity exceeds a critical value, namely, $\sqrt{T_b/\rho}$, with the possible formation of shocks in the cable.

The vector-valued eigenfunction $(X(s), Z(s), T(s))$, solution of the eigenproblem (28), is defined up to an arbitrary scalar multiplicative coefficient. A possible choice for such constant is to require that the Euclidean norm equals 1, namely,

$$||(X(s), Z(s), T(s))|| \equiv \int_0^1 \sqrt{X(s)^2 + Z(s)^2 + T(s)^2}\mathrm{d}s = 1. \tag{32}$$

Since the perturbation $\varepsilon(X(s), Z(s), T(s))\mathrm{e}^{I\omega t}$ is expected to be smaller than the static solution $(X_0(s), Z_0(s), T_0(s))$, we can pose $\varepsilon \frac{||(X(s),Z(s),T(s))||}{||(X_0(s),Z_0(s),T_0(s))||} \ll 1$ which, combined with Eq. 32, yields $\varepsilon \ll ||(X_0(s), Z_0(s), T_0(s))||$ where the expected *smallness* can be quantified by setting $\bar{\varepsilon} = 10^{-2}$ in the following:

$$\varepsilon < \bar{\varepsilon}\, ||(X_0(s), Z_0(s), T_0(s))|| = \bar{\varepsilon}\, S(\Gamma), \tag{33}$$

where the function $S(\Gamma) \equiv ||(X_0(s), Z_0(s), T_0(s))||$ can be readily obtained by expressing the static solutions in Eq. 10 as functions of Γ. The ratio of the velocity of the seabed point to the characteristic value $\sqrt{T_b/\rho}$ can be formulated from Eq. 15 and, after straightforward algebraic manipulation, is given by $\left|\frac{s_b'(t)}{\sqrt{\frac{T_b}{\rho}}}\right| = \varepsilon\omega \left|Z'(0)\right| \sqrt{\Gamma}$ where all quantities on the right-hand side are to be understood as nondimensional.

For the evaluation of the above ratio, the numerical approach discussed in Sect. 5 has been employed for various Γ values. In Fig. 5 we plot the curves $\varepsilon G_i(\Gamma) = 1$ in the (Γ, ε) plane for the first three modes ($i = 1...3$), where $G_i(\Gamma) \equiv \omega_i \left|Z_i'(0)\right| \sqrt{\Gamma}$. The regions below these curves correspond to shock-free solutions for the eigenproblem,

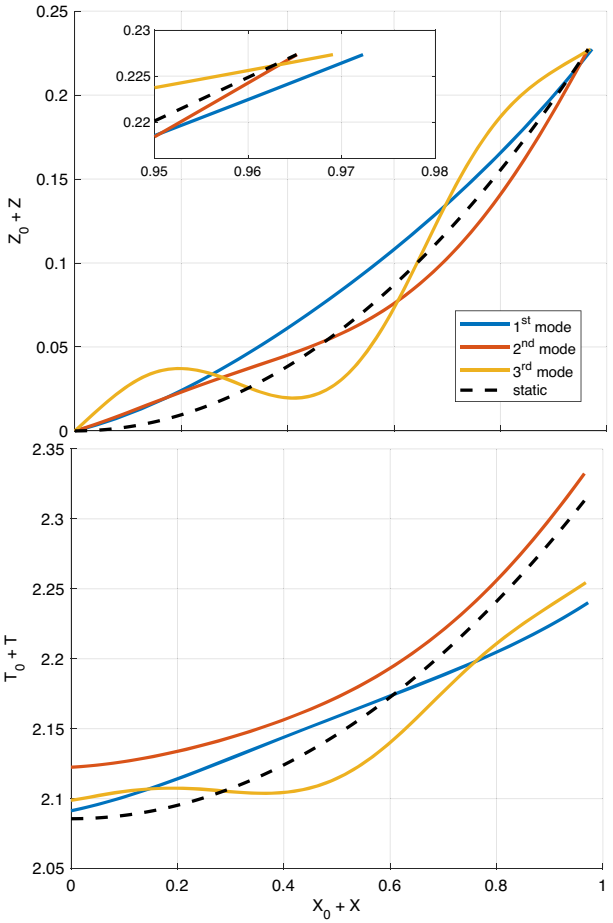

Fig. 3 Top and bottom panels show, respectively, the first three eigenmodes, for $\beta = 4.4$. The static reference shape is shown as well. The inset of the top panel shows the different displacement of the fairlead point in the different modes

namely $\left| s_{\mathrm{b}}'(t) / \sqrt{\frac{T_{\mathrm{b}}}{\rho}} \right| < 1$. The above analysis shows that exceeding the limiting speed at the seabed contact point depends on the amplitude of the perturbed solution ϵ, the nondimensional tension Γ, and the mode number. Since a higher mode number entails a larger pulsation and therefore a higher seabed contact point velocity, one would expect the admissible regions to shrink with increasing mode number. This is not the case here: the third mode is indeed the most restrictive, but the second one bounds the largest admissible, shock-free region. This non-trivial ranking can be explained by noting that the eigenmode profile for the second mode (see the inset in the top panel of Fig. 3) exhibits the smallest oscillation at the fairlead, thus inducing slower oscillations of the seabed contact point. The admissible regions must be further restricted by noting that not all shock-free solutions comply with the requirement of *small* perturbations of the static configuration, as prescribed by the constraint in Eq. 33. Only the points

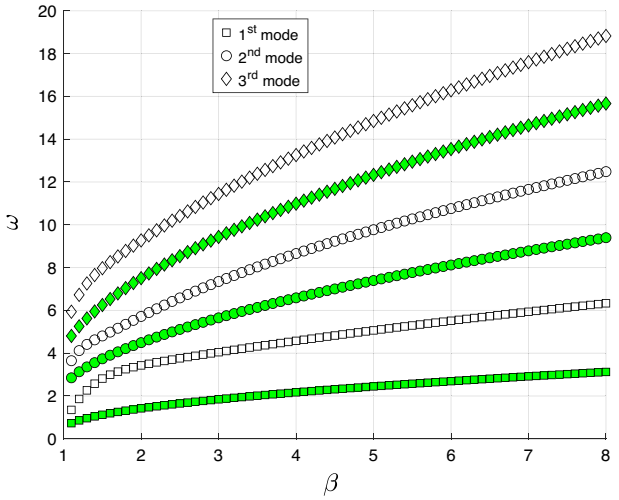

Fig. 4 First three natural pulsations as predicted by the modal analysis. Green-filled marker refers to the results obtained with the assumption of negligible departure of tension from the static value

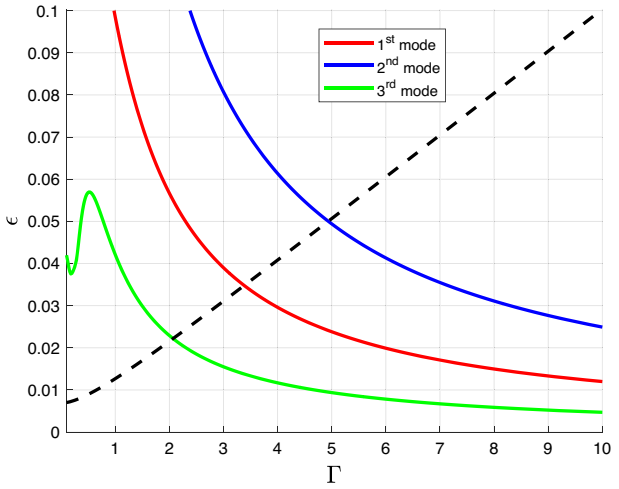

Fig. 5 Shock-free regions for the modal analysis: each solid trace represents the upper bound for the existence of a perturbed solution which does not trigger shocks due to a fast moving seabed contact point. The dashed line indicates the limit for small perturbations, assuming $\overline{\varepsilon} = 10^{-2}$ in Eq. 33

below the dashed line in Fig. 5 can thus be regarded as *small*, according to the assumed value for $\overline{\varepsilon} = 10^{-2}$.

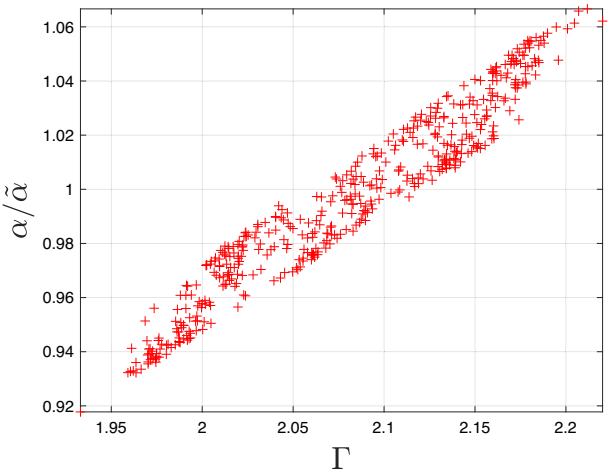

Fig. 6 Values attained by the angle α between the seabed and the segment passing through the two line extrema, normalized with its static value $\tilde{\alpha}$, during a typical time-varying simulation, versus the corresponding Γ values

7.2 Free oscillations in the time domain: influence of the seabed boundary condition.

We solved the dynamic equation (23) by means of the numerical method described in Sect. 6. In particular, after initiating the profile according to the static solution equation (24), we imposed a step variation of the fairlead tension, which eventually triggered free oscillations of the whole line. Then, we extracted the spectrum of the time series of the position of the fairlead, as shown in Fig. 7, for both implementation strategies of the boundary condition at the seabed. The two spectra show very close peaks, with the rigorous condition yielding values more adherent to the reference values of the modal analysis, the latter reported in Fig. 7 as vertical lines. Moreover, the empirical description of the seabed contact results in a spectrum with a lower number of detectable peaks. This occurs because the reduced stability induced by such a naive boundary condition requires the use of a smaller time step, resulting in higher numerical dispersion and, consequently, smearing of higher-frequency waves due to increased phase errors and, thus, destructive interference.

While the natural frequencies yielded by the empirical description of the seabed dynamics satisfactorily approximate the ones predicted by the modal analysis, the mean displacement is poorly approximated, as shown in the next section. It is interesting to inspect the values attained, during a typical time-varying simulation, by the angle α between the seabed and the segment passing through the two line extrema. Figure 6 shows the cloud of such angles, normalized by the critical (static) value as in Eq. 27, as a function of Γ. It is worth mentioning that both quantities vary in time, though α shows small departures from the critical value, as expected for a simulation setup to assess the natural frequencies of the system.

Building upon the static equations (24), an explicit formulation for the displacement of the TDP between two static configurations has been reported in Appendix B. Such quasi-static transitioning from the initial to the final state can be employed as the reference value for the mean location of the TDP oscillation, as predicted by the dynamic equations. As shown in Fig. 8, the comparison highlights that the prediction strongly depends on the choice of the boundary condition. Implementing the correct boundary condition (Eq. 6) yields significantly more accurate results: indeed, the associated error is approximately 1%, whereas the empirical seabed condition leads to a discrepancy of about 15%. This is certainly to be considered a lower boundary since the free oscillations are obtained by solving the dynamic equation (23) with a small variation of the fairlead tension, in the order of 10%. Higher errors are expected in presence of larger variations: indeed, as shown in Fig. 9, small variations of the location of the fairlead point reflect into considerably larger displacements of the TDP.

Future research will seek to elucidate the extent to which discrepancies in the replication of experimental data reported by several authors can be attributed to the utilization of simplified seabed boundary conditions.

8 Conclusions

A modal analysis of the slack configuration of a mooring line has been carried out, with focus on the role of the seabed boundary condition (TDP). An exact, simple differential formulation has been rigorously derived for the dynamic displacement of the TDP. Such condition, once implemented in the time-varying equations, yields oscillations that closely reproduce both the frequency of the modal analysis, and the mean displacement of the TDP. The empirical condition of line-seabed contact, on the contrary, yields inaccurate predictions of the TDP location. Since the residual available resistance of a slack mooring heavily depends on the amount of line lying on the seabed, accurately predicting the TDP displacement is crucial for correctly estimating the ultimate stability of the mooring. The present study highlights the importance of a consistent modeling approach for the TDP condition within a modal framework. Numerical results from time-varying simulations, although performed in small-oscillation regimes, suggest that the above conclusions may also extend to more realistic scenarios. Further investigations are, however, required to confirm this indication.

Author contributions P.P. and G.S. contributed equally to this work.

Funding Open access funding provided by Università degli Studi Roma Tre within the CRUI-CARE Agreement.

Data availability No datasets were generated or analyzed during the current study.

Declarations

Conflict of interest The authors declare no conflict of interest.

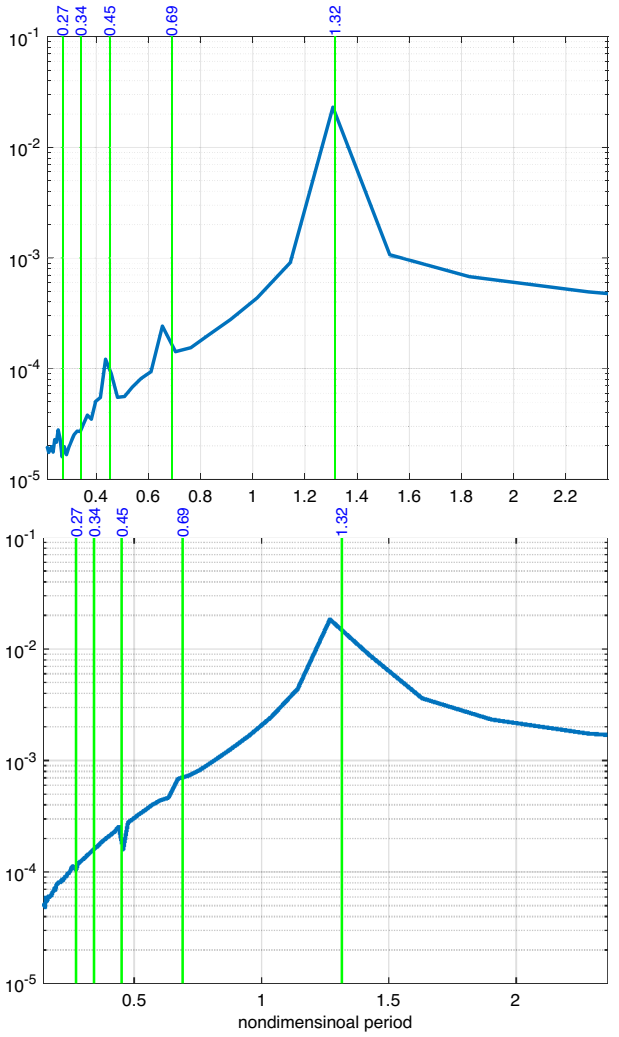

Fig. 7 Spectra of the oscillation of the position of the fairlead; rigorous seabed boundary condition as in Eq. 6 (upper panel) and empirical description of the seabed contact (lower panel). Green vertical lines and corresponding values are the first five eigenvalues resulting from the modal analysis

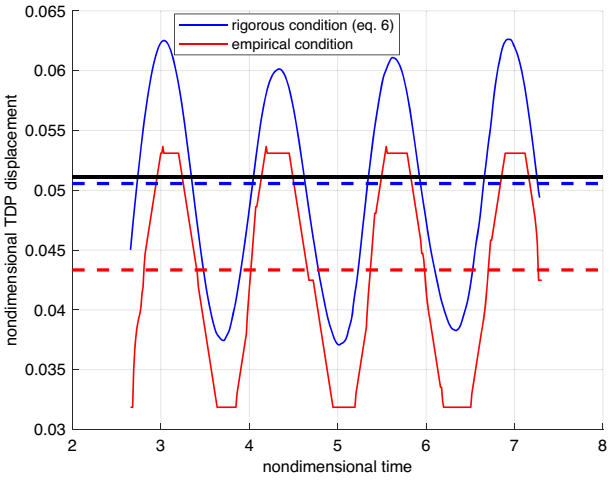

Fig. 8 Dynamic modeling: oscillation of the TDP consequent to a drop in tension at the fairlead (nondimensional T_f varies from 2.2 to 2.1). Comparison between the rigorous boundary condition (Eq. 6) and the empirical seabed condition. Mean values are also shown in dashed lines and can be compared to the location of the TDP as predicted by the quasi-static displacement Eq. B1 for $\beta_{0,A} = 4.622$ and $\beta_{0,B} = 4.399$ (black trace)

Appendix A Variational formulation of the problem

In this section, we show how Eqs. 2 and 8 can be derived from the principle of least-action. The action of a line subject to a conservative mass force $\mathbf{f}$ whose potential energy is $\Phi(\mathbf{X})$, can be formulated as $\mathcal{A}[\mathbf{X}, T] = \int_{t_0}^{t_1} \left[\int_{s_\mathrm{b}(t)}^{s_\mathrm{f}} \mathcal{L}\, \mathrm{d}s + L_\mathrm{f}(t) \right] \mathrm{d}t$, where $\mathcal{L} = \frac{1}{2}\rho\,|\mathbf{X}_t|^2 - \rho\Phi(\mathbf{X}) - \frac{1}{2}T\left(|\mathbf{X}_s|^2 - 1\right)$ is the lagrangian density, and $L_\mathrm{f}(t) = T_\mathrm{f}(t)x(s_\mathrm{f}, t)$ is the generalized potential of the external tension applied at the fairlead. It is worth noting that the tension at the TDP $T_\mathrm{b}(t)\boldsymbol{\tau}(s_\mathrm{b}, t)$ is assumed to be horizontal, and thus the TDP detaches from the bottom with purely vertical velocity, that is $x_t(s_\mathrm{b}(t), t) = 0$ owing to $x(s_\mathrm{b}(t), t) = s_\mathrm{b}(t)$ and $x_s(s_\mathrm{b}(t), t) = 1$. Therefore no work is performed by the tension $T_\mathrm{b}(t)$, and thus it does not appear in the above action budget. To come to the hamiltonian formulation we define the $\mathbf{X}$ conjugate moment as $\mathbf{P} \equiv \partial\mathcal{L}/\partial\mathbf{X}_t = \rho\mathbf{X}_t \Rightarrow \mathbf{X}_t = \mathbf{P}/\rho$. By applying the Legendre transform, the hamiltonian reads $\mathcal{H}[\mathbf{P}, \mathbf{X}, T] = \int_{s_\mathrm{b}(t)}^{s_\mathrm{f}} \left(\frac{1}{2\rho}\,|\mathbf{P}|^2 + \rho\Phi(\mathbf{X}) + \frac{1}{2}T\,(|\mathbf{X}_s| - 1) \right) \mathrm{d}s - L_\mathrm{f}(t)$, with T as a Lagrange multiplier. The field equations on the open interval $(s_\mathrm{b}(t), s_\mathrm{f})$ together with the boundary condition $Tx_\mathrm{s} = T_\mathrm{f}(t)$ at $s = s_\mathrm{f}$ are obtained through a standard procedure of minimization of the action with respect to $\mathbf{X}$ and T, with the following admissible variations: $\delta\mathbf{X}(\cdot, t_{0,1}) = \mathbf{0}$, $\delta\mathbf{X}(s_\mathrm{b}, t) = \mathbf{0}$, $\delta\mathbf{X}(s_\mathrm{f}, t) = \{\delta x(s_\mathrm{f}, t), 0\}$. In particular, by imposing $\delta_\mathbf{X}\mathcal{A} = 0$ we can derive both the momentum balance and the boundary condition $Tx_\mathrm{s} = T_\mathrm{f}$ while the prescription $\delta_T\mathcal{A} = 0$ leads to the inextensibility constraint. In the Hamiltonian framework, the same equations follow from admissible variations with respect to $\mathbf{X}$, $\mathbf{P}$, and T. The kinematic law

governing $s_b(t)$ (see Eq. 6) cannot be derived within the present variational setting and needs to be prescribed externally.

Appendix B "Static" displacement of TDP

.5ptIn this section, we derive a relation linking the displacement of the TDP, Δs_b, to that of the fairlead point, Δx_f, the latter induced by a variation in the applied tension. Assuming a slow variation of the tension from a state A to a state B, the results are strictly valid in a quasi-steady setting. If the nondimensional fairlead tension varies from $\Gamma_{0,A} \rightarrow \Gamma_{0,B}$ where $\Gamma_{0,A} = T_{f,A}/(\rho g L_A)$ and $\Gamma_{0,B} = T_{f,B}/(\rho g L_A)$, it is worth recalling that, in a static slack-line configuration, the horizontal component of the fairlead tension equals the tension at the TDP. The displacement of the TDP equals the variation of the suspended line from state A to state B, namely $\Delta s_b = \Delta L = L_B - L_A \gtrless 0$. It can be determined by imposing that, at both states, the fairlead moves only horizontally, namely, $Z_0(L_A) = Z_0(L_B) = h$. Solving for $s = L_A$ and $s = L_B$ the first of Eq. 10 $L_A = \sqrt{h\,(2\chi_A + h)}$, $L_B = \sqrt{h\,(2\chi_B + h)}$, which allows formulating the nondimensional variation of L as $\frac{\Delta L}{L_A} = \sqrt{\frac{\frac{2\chi_B}{h}+1}{2\chi_A/h+1}\frac{2\chi_A}{h} + 1} - 1$. The previous relation, considering that $\chi = \Gamma L$ and accounting for Eq. 26, can be written as

$$\begin{aligned} \Delta s_b/h &= \beta_{0,A} - \beta_{0,B}, \\ \Delta x_f/h &= \Delta s_b/h + \ln \sqrt{\left(\frac{\beta_{0,B}+1}{\beta_{0,B}-1}\right)^{\beta_{0,B}^2-1} \left(\frac{\beta_{0,A}-1}{\beta_{0,A}+1}\right)^{\beta_{0,A}^2-1}}, \end{aligned} \tag{B1}$$

where the variation in tension reflects in the variation $\beta_{0,A} \rightarrow \beta_{0,B}$.

The above relations can be employed to draw the parametric plot in Fig. 9, which readily provides a means to assess the residual stability of a mooring system: indeed, the length variation of the suspended portion of the mooring line can be estimated based on the local depth and the displacement of the fairlead.

References

1. Walton TS, Polachek H (1960) Calculation of transient motion of submerged cables. Math Comput 14(69):27–46
2. Burridge R, Keller JB (1978) Peeling, slipping and cracking - some one-dimensional free-boundary problems in mechanics. SIAM Rev 20(1):31–61
3. Nakajima T, Motora S, Fujino M (1982) On the dynamic analysis of multi-component mooring lines. In: Offshore technology conference 4309 OTC
4. Garza-Rios LO, Bernitsas MM, Nishimoto K (1997) Catenary mooring lines with nonlinear drag and touchdown. Technical Report Publication No. 333, University of Michigan, Department of Naval Architecture and Marine Engineering, Ann Arbor (January 1997). Prepared for the University of Michigan/Industry Consortium in Offshore Engineering
5. Gobat JI, Grosenbaugh MA (2001) Dynamics in the touchdown region of catenary moorings. Int J Offshore Polar Eng 11(4):273–281
6. Batista M, Perkovič M (2019) Computation of mooring chain with the touchdown on an inclined seabed. J Mar Eng Technol 21(1):9–22

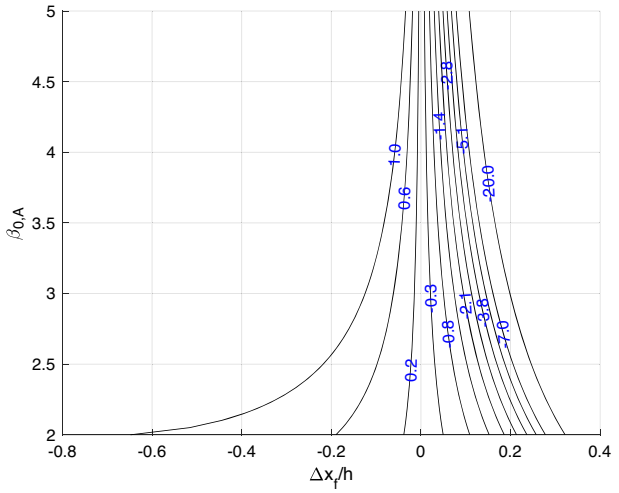

Fig. 9 Plot of iso-$\Delta s_b/h$ curves (blue values) as functions of the initial configuration $\beta_{0,A}$ and the movement of the fairlead point $\Delta x_f/h$. For any $\beta_{0,A}$, small variations of the fairlead position induce large movement of the TDP location, thus further substantiating the importance of a correct modeling of the latter

7. Mohapatra SC, Soares CG (2021) Effect of mooring lines on the hydroelastic response of a floating flexible plate using the Biem approach. J Mar Sci Eng 9(9):94
8. Desiré P, Rodríguez-Luis Á, Guanche R (2023) Simulation of mooring lines in complex bathymetries using a finite element method. Ocean Eng 272:113827
9. Amouzadrad P, Mohapatra SC, Guedes Soares C (2026) Analytical and numerical model on the hydroelastic response of an array of moored circular offshore floating platform. Ocean Eng 343:123316
10. Liu Y, Sun R, Cao H, Wan D (2013) Motion response analysis of a semi-submersible platform with catenary mooring system. In: Proceedings of the eighth international workshop on ship hydrodynamics, Seoul, Korea
11. Chang A, Wang S, Du J, Li H (2019) Second-order frequency-domain coupled analysis for moored offshore structure dynamics. Ocean Eng 174:201–215
12. Ma K-t, Shu H, Smedley P, L'Hostis D, Duggal A (2013) A historical review on integrity issues of permanent mooring systems. In: Offshore technology conference (OTC), p 24025
13. Kvitrud A (2014) Lessons learned from Norwegian mooring line failures 2010–2013. In: International conference on offshore mechanics and Arctic engineering, vol 45424. American Society of Mechanical Engineers, p 04-02005
14. Liu Y, Bergdahl L (1997) Frequency-domain dynamic analysis of cables. Eng Struct 19:499–509
15. Papazoglou VJ, Mavrakos SA, Triantafyllou MS (1990) Non-linear cable response and model testing in water. J Sound Vib 140(1):103–115
16. Triantafyllou MS, Bliek A, Burgess J, Shin H (1986) Mooring dynamics for offshore applications. Part I, Theory. Technical Report MITSG 86-1, MIT Sea Grant College Program, Massachusetts Institute of Technology, Cambridge. Supported by NOAA Sea Grant and NAVSEA
17. Thomas DO (1993) A numerical investigation of time integration schemes applied to the dynamic solution of mooring lines. PhD thesis, Newcastle University, Newcastle upon Tyne; includes study of Central Difference, Houbolt, Wilson-θ, Newmark schemes
18. Gobat JI (2000) The dynamics of geometrically compliant mooring systems. PhD thesis, Massachusetts Institute of Technology and Woods Hole Oceanographic Institution, Cambridge. Advisor: Grosenbaugh MA
19. Gao Y, Guo C, Wang L, Lin P (2021) Experimental investigation on responses characteristics of a mooring line with imposed top-end motions. Ocean Eng 229:108980
20. Srinil N, Rega G, Chucheepsakul S (2007) Two-to-one resonant multi-modal dynamics of horizontal/inclined cables. Part I: theoretical formulation and model validation. Nonlinear Dyn 48(3):231–252

21. Goswami B, Chakraborty I, Chatterjee A (2025) Small in-plane oscillations of a slack catenary using assumed modes. J Vib Eng Technol 13(6):1–8
22. Wang J, Cao G, Zhu Z, Wang Y, Peng W (2015) Lateral response of cable-guided hoisting system with time-varying length: theoretical model and dynamics simulation verification. Proc Inst Mech Eng C J Mech Eng Sci 229(16):2908–2920
23. Zhong W, Zhao W, Wan D, Zhao Y (2024) Comparison study on mooring line models for hydrodynamic performances of floating offshore wind turbines. Ocean Eng 296:117083
24. Kurian VJ, Yassir MA, Ng CY, Harahap IS (2013) Nonlinear dynamic analysis of multi-component mooring lines incorporating line-seabed interaction. Res J Appl Sci Eng Technol 6(14):1428–1445
25. Palm J, Eskilsson CG, Bergdahl L (2017) An HP-adaptive discontinuous Galerkin method for modelling snap loads in mooring cables. Ocean Eng 144:266–276
26. Governo A, Henriques J, Gato L (2023) Modelling mooring line snap loads using a high-order finite-volume approach. Ocean Eng 275:113803
27. Saad Y (2011) Numerical methods for large eigenvalue problems, 2nd edn. Society for Industrial and Applied Mathematics, Philadelphia